Journal of Instrumentation

PAPER • **OPEN ACCESS**

Beam emission spectroscopy diagnostic design and capabilities for two-dimensional turbulence measurements on Wendelstein 7-X

To cite this article: X. Han *et al* 2024 *JINST* **19** P11004

Published by IOP Publishing for Sissa Medialab

Received: *June 5, 2024*
Revised: *October 2, 2024*
Accepted: *October 22, 2024*
Published: *November 13, 2024*

Beam emission spectroscopy diagnostic design and capabilities for two-dimensional turbulence measurements on Wendelstein 7-X

X. Han,[a,*] **D. R. Smith**,[a] **T. Windisch**,[b] **R. Laube**,[b] **D. Den Hartog**,[a] **C. Seyfert**,[a] **T. Gallenberger**,[a] **K. Jaehnig**,[a] **B. Geiger**,[a] **G. McKee**,[a] **O. Grulke**[b,c] **and the Wendelstein 7-X team**[1]

[a] *University of Wisconsin-Madison, Madison, Wisconsin 53706, U.S.A.*
[b] *Max-Planck-Institut für Plasmaphysik, 17491 Greifswald, Germany*
[c] *Technical University of Denmark, Kongens Lyngby, Denmark*

E-mail: xiang.han@wisc.edu

Abstract: A beam emission spectroscopy (BES) diagnostic is designed for studying two-dimensional turbulent dynamics by measuring the Doppler-shifted Balmer-Alpha emission ($n = 3 \rightarrow 2$) from neutral heating beams on Wendelstein 7-X (W7-X) stellarator. The BES viewing geometry has been determined in the conceptual design previously. However, the small Doppler shifts and small optical throughput compared to a typical BES diagnostic demand dedicated efforts on the optical assemblies and the detector module for the BES system. We present the detailed opto-mechanical design and specifications of BES, including a customized neutral beam viewing optical system, a semi-telecentric optical assembly, and a detector module for electronic amplification. The point spread function is calculated using the pyFIDASIM code with experimental parameters and W7-X magnetic configurations to estimate the BES spatial resolution and beam intensity. The as-manufactured interference filter is applied for the spectral isolated beam radiance calculation. Result shows that the BES system is capable of measuring the ion-scale turbulence for $k_\perp \rho_i \leq 0.4$ at $r/a = 0.75$ with reasonable spatial and wavenumber resolutions. An integrated detector module is fabricated where two 8×4 avalanche photodiode detectors (APD) are embedded into the custom-designed pre-amplifier circuit to gain signals to the desired level. The detector noise measurement is performed and the signal-to-noise ratio (SNR) is evaluated. A detectable fluctuation level can be achieved as low as $\tilde{n}_e/n_e \approx 0.5\%$ at frequency $f \leq 400\,\text{kHz}$ with a bandwidth of 1 MHz.

Keywords: Nuclear instruments and methods for hot plasma diagnostics; Plasma diagnostics - interferometry, spectroscopy and imaging; Detector design and construction technologies and materials

*Corresponding author.

[1] See Sunn Pedersen et al. 2022 (https://doi.org/10.1088/1741-4326/ac2cf5) for the W7-X Team.

https://doi.org/10.1088/1748-0221/19/11/P11004

Contents

1 Introduction

Turbulent transport driven by the ion temperature gradient (ITG) and/or trapped electron mode (TEM) is found to play a significant role in plasma confinement in the Wendelstein 7-X (W7-X) stellarator [1–3] due to the fact that anomalous transport in the ion gyroradius scale primarily limits the performance of neoclassical transport reduction that is observed in pellet-fueled discharges on W7-X [4, 5]. A novel Beam Emission Spectroscopy (BES) diagnostic is designed for the 2-dimensional (2D) density and flow field fluctuation measurements aiming to investigate the role of turbulence with multi-scale interactions on the particle transport on W7-X.

BES diagnostic measures the volume-sampled density fluctuation imprinted in the emission of the neutral heating beam, where the density fluctuation $\tilde{n}_e/n_e$ is proportional to the intensity of beam emission as $\tilde{n}_e/n_e = C\tilde{I}/I$ [6]. The $\tilde{I}/I$ is the isolated spectral emission of the Doppler-shifted Balmer-α emission ($n = 3 \longrightarrow 2$ at $\lambda_0 \approx 656.3$ nm for hydrogen) that is collisionally excited from the neutral heating beam [7]. The constant C depends on multiple parameters and is approximately equal to $2 \sim 3$ [8]. An advanced feature of the BES diagnostic is the ability to present two-dimensional turbulent image with high spatial and temporal resolution (in μs range) hence to measure the transient event like edge-localized modes (ELMs) or sawtooth [9]. Moreover, turbulence properties such as correlation length, decorrelation rate, turbulent velocity field, and Reynolds stress can be characterized. The BES diagnostic has been implemented in many fusion experiments for turbulent image measurements such as DIII-D [10, 11], NSTX [12], HL-2A [13–15], MAST [16], and LHD [17].

The viewing geometry of the BES system has been previously determined in the conceptual design by a comprehensive comparison of beam-LoS configurations and port availability [18]. The radial coverage of $r/a \sim 0.5$–1.2 is preferable for the scientific motivation of BES. A vertical port (AEW30) in the triangular cross-section is selected to implement the beam viewing optic for congregating the fluorescence from the neutral heating beam source 7. However, the BES viewing geometry at the AEW30 port indicates a small Doppler shift and a small amount of optical throughput comparing with a typical BES diagnostic. Therefore the optical assembly and the detector module need to be customized

2024 JINST 19 P11004

with dedicated efforts in order to accommodate the ITG/TEM turbulence measurements with the BES diagnostic. In addition, it is necessary to assess the BES performance thoroughly with various magnetic configurations and operational regimes of W7-X for an optimization of the BES diagnostic.

In this paper, we present the progress of the BES system and assess its capability for turbulence measurements. In the remainder of the paper, the beam viewing optical assembly at the AEW30 port and the semi-telecentric optical assembly at the detector-end are described in section 2, the detector module is shown in section 3, the Point Spread Function (PSF) and Spatial Transfer Function (STF) are calculated in section 4, the beam radiance and detector noise level are estimated in section 5. In the summary 6, the BES capabilities for the ion-scale turbulence imaging measurement is evaluated.

2 BES optical assemblies

2.1 Beam viewing optical assembly

The field of view of BES diagnostic requires a distinguishable Doppler-shifted beam emission that is isolated from edge recycling and thermal charge-exchanged (CX) emissions. Meanwhile, a field-aligned line-of-sight (LoS) is highly demanded for the purpose of minimizing the spatial smearing effect of turbulent eddies. Figure 1 shows the BES viewing geometry at AEW30 port (toroidal angle $\phi \approx 108.9°$) that collects the beam emission from the neutral beam source 7 at $\phi \approx 87°$. This field of view provides a good field alignment in the plasma edge region, and fulfills the region of interest for studies of ITG/TEM turbulence and anomalous transport.

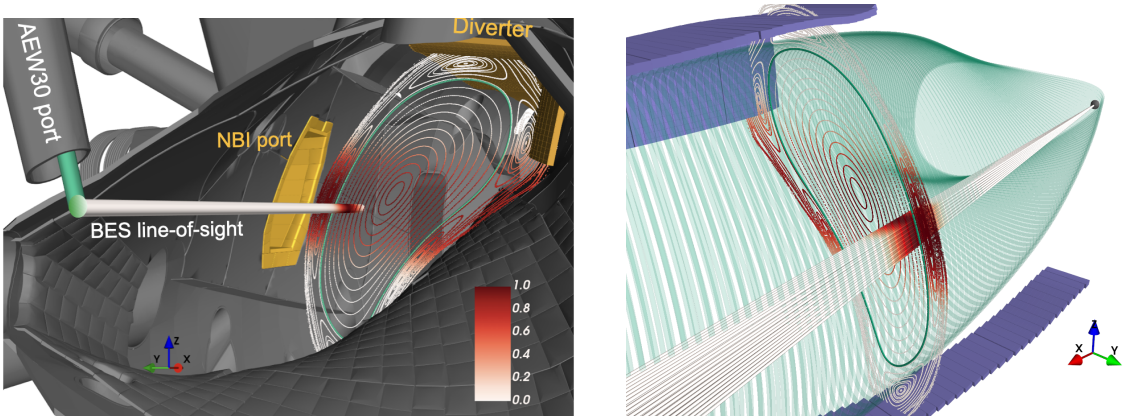

(a) BES field of view in the vacuum vessel of W7-X.

(b) Isometric view of the BES viewing geometry.

Figure 1. The BES field of view in the vacuum of W7-X. The NBI source 7 is located at the yellow port of (a), where the Poincaré figure in the standard magnetic configuration (EJM+252) is depicted with the normalized beam density scaled by the color range. and the green fluxsurface indicates the last closed fluxsurface. The collected beam is reflected through the AEW30 port where the reflected beam is depicted in the green tube, whereas the white tube shows the light cone that is intersected with the neutral beam volume. Note the beam density along the light cone is scaled by the same color range. The heat shield and the mirror structure are not shown in (a). (b) the isometric view of the BES viewing geometry from the other side of the beam volume. The last closed flux surface is indicated in green, and the divertor targets are depicted in purple. The parking position of the mirror is shown by the grey spot.

Figure 2 calculates the Doppler shifts, neutral beam density, and the magnetic field angle at the cross section of the neutral beam axis in the standard magnetic configuration (EJM+252). The BES

2024 JINST 19 P11004

field of view is rotated poloidally in order to match the normal and bi-normal directions of the magnetic field. The D_α emission is blue-shifted by 1.5 $\sim$ 2 nm with respect to the Balmer-emission line from hydrogen at 656.3 nm. The small Doppler shift is constrained by the radial heating beam corresponding to a nearly perpendicular field of view from the AEW30 port. In figure 2(b) the neutral beam density is calculated using plasma parameters from a representative discharge with neutral beam injection (NBI) on W7-X. Moreover, in figure 2(c), it is shown the angle between BES field of view and the magnetic field is as low as 4° $\sim$ 6°, indicating a field-aligned LoS of the BES. By comparing the Doppler shift, the neutral beam density, and the angle of magnetic field in figure 2, it is concluded that the BES field of view at the outer mid-plane is well preserved for a sufficient beam intensity in the plasma edge region.

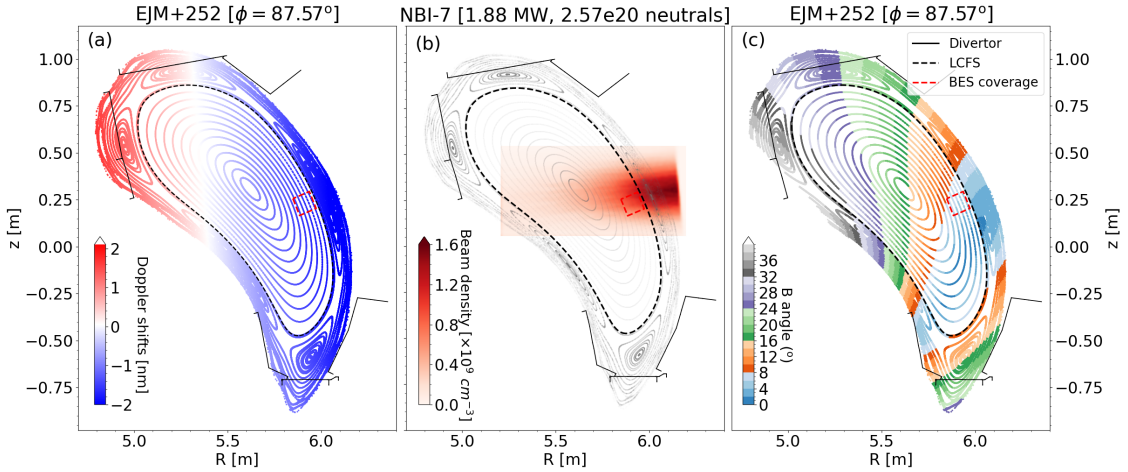

Figure 2. (a) The Doppler shifts calculation at the ϕ = 87.57° cross section of neutral beam source 7 in the EJM+252 configuration. The last-closed flux surface (LCFS) is indicated by the black dashed line, and the BES coverage is depicted by the red dashed area. (b) The Poincaré figure on the beam axis is shown in gray, and the beam density is calculated using the pyFIDASIM code with the plasma parameters from an NBI discharge 20180919.039. (c) The magnetic field angle calculation in the EJM configuration with respect to the BES field of view.

A neutral beam viewing optical assembly is custom-designed to accommodate optical components and fiber through the AEW30 port. This is a retractable optical assembly consisting of an elliptical mirror, an integrated heat shield structure, and a periscope that contains a vacuum window and multiple lenses. The heat shield is mounted behind the mirror and is actively water cooled to handle the heat load from plasma. The front shape follows the curvature of the surrounding graphite tiles to avoid any leading edges. A mechanical design of the beam viewing optical assembly is shown in figure 3, where light from plasma is reflected by the mirror and collimated through the periscope to the fiber terminal on the image plane. The fiber terminal consists of an 8×8 optical fiber array (1500 µm core diameter, NA = 0.22, core-to-core spacing at 1560 µm), whose interface is placed on the image plane of the periscope to deliver the light to the semi-telecentric optical assembly and the detector module. The mirror is tilted 114.8 degrees with respect to the lens axis to reflect the light towards the lenses and fiber array. The size of the mirror is maximized to avoid the clipping of the different light ray bundles by this mirror. During the plasma operation, the mirror and heat shield are outstretched at the fixed position. The footprint of the beam on the mirror is calculated in figure 3 using this optical assembly. Although the footprint moves toward the mirror edge for the corner positions of the 8×8 fiber array, the minimum distance to the mirror edge is about 0.8 mm

2024 JINST 19 P11004

for the outermost positions. In case of damage during operation, a 10×10 fiber array is prepared and the outermost fibers are spare to replace those broken fibers.

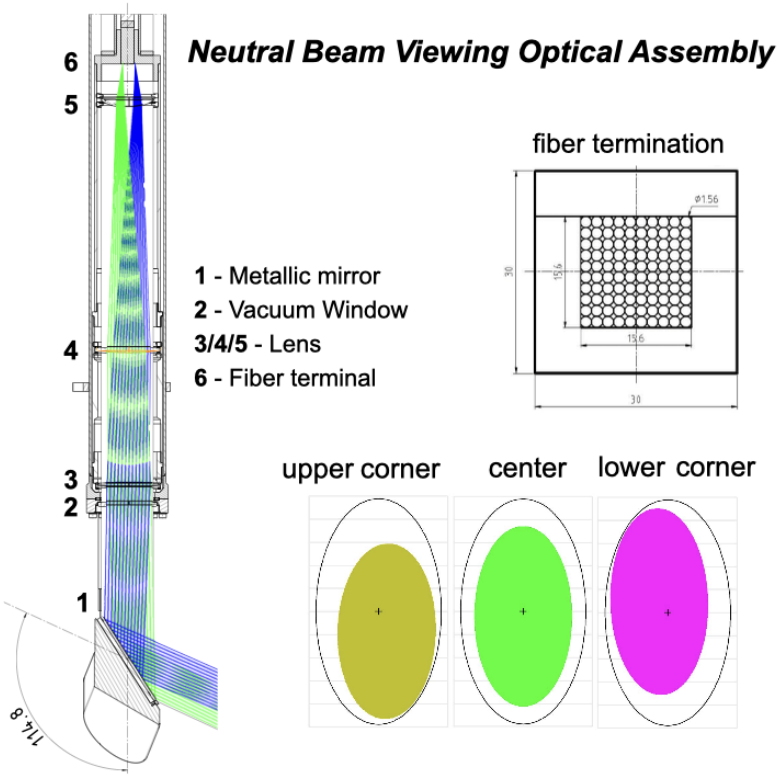

Figure 3. Layout of components in the neutral beam viewing optical assembly at the AEW30 port, where the components are indicated by the numbers on the left. The elliptical mirror is tilted 114.8 degrees towards the lenses and the fiber terminal. The blue and green rays are two of the beams at the outermost pixel on the fiber termination. The footprints of the beam on the mirror for three pixels are shown on the lower right. The fiber termination layout is depicted on the upper right. Note it is a 10×10 fiber array where the outermost fibers are spare and can replace the broken fibers when damaged.

A transparent indium tin oxide (ITO) is coated on the vacuum window to block the stray radiation from the electron cyclotron resonance heating (ECRH). In the periscope system, a biconvex lens (f = 750 mm, clear aperture = 54 mm) is positioned behind the vacuum window, which is the limiting aperture to determine the optical throughput (or étendue). Then the beam passes through two plano-convex lenses to be focused on the optical fiber terminal on the image plane. A spatial adjustment is possible to orient the fiber surface plane. This beam viewing optics provides a roughly 1 to 10 magnification from the fiber terminal to the object plane in the plasma, that exhibits an observed spot size of about 15 mm diameter for each 1500 µm core fiber focused on the neutral beam axis. Thus, the 8×8 fiber array forms a rectangular area with the width of 12.48 mm. The étendue calculation resolves the beam radiance that passes through the BES optical assembly, hence determining the minimum fluctuation level that can be detected. The étendue is estimated by taking into account the size of the fiber image, the distance from the beam axis to the biconvex lens (about 2.4 m). Considering a 1.56 cm spacing between two adjacent spots on the object plane and a 5.4 cm diameter clear aperture of the biconvex lens, the optical throughput is about 0.07 $\text{mm}^2 \cdot \text{ster}$.

2024 JINST 19 P11004

2.2 Semi-telecentric optical assembly at the detector-end

The fiber array transmits the light from the beam viewing optical assembly to the remotely located detector module, where the spectral isolated beam emission is examined via a semi-telecentric optical assembly and a customized detector for the electronic amplification. The semi-telecentric optical assembly is custom-designed for light collimation and band-pass filtering the beam emission from the fiber termination. The 8×8 fiber array from the AEW30 port is split into 64 individual fibers to be positioned on the object plane of the semi-telecentric optical assembly, where all fibers are collimated through holes on an 8×8 grid. Figure 4(b) shows the semi-telecentric optical assembly and the integrated detector module. The positions of lenses are optimized to minimize the light loss arising from the light vignetting or spreading outside the pixel boundary. The f-number of the light collection is designed at $f/4.2$ resulting in unity lateral magnification for the fiber-to-pixel imaging. The interference filter is inserted at the conjugate focal plane separating the object and image lens units. The cut-off wavelength of the interference filter is carefully determined so as to maintain the beam energy components in the pass-band while minimizing the spectral contamination from the undesired emission. Although a sharp cutoff edge of the filter is desired, a small fraction of thermal CX emission remains in the pass band due to the small Doppler shifts and the effect of angle-of-incidence (AOI) on down-shifting the pass-band of the filter. The most off-axis pixels possess a maximum AOI of around 4°, which could downshift the pass-band of the interference filter by about 0.4 nm. This interference filter is manufactured as an ultra-narrow band-pass filter (full width at half maximum (FWHM) is about 3.29 nm) whose 90% transmission ranges from 653 to 655.3 nm and the 10% cut-off is at 655.7 nm. The optical density (OD) at 656.3 nm is greater than 5 for both 0° and 4° AOI which is sufficient to block the thermal charge-exchanged emission at 656.3 nm.

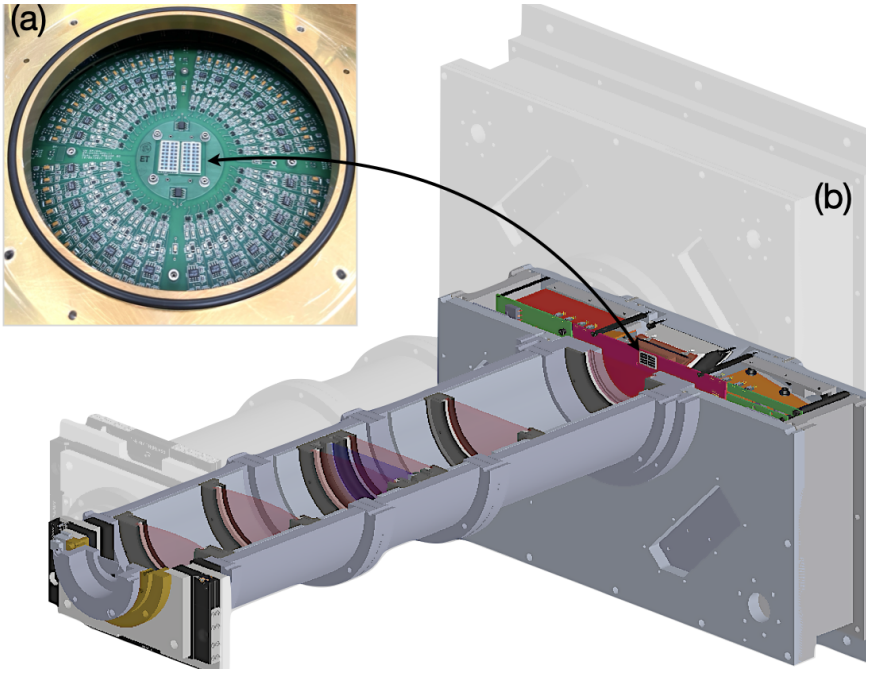

Figure 4. (a) the picture of the APD diode array and the pre-amplifier circuit. (b) The optical lens assembly that is mounted in front of the APD array. The cross sections of lenses are positioned in red in the lens assembly, and the interference filter is inserted in blue.

2024 JINST 19 P11004

3 BES detector module

On the image plane of the optical assembly, two avalanche photodiode (APD) arrays from Hamamatsu (S8550-02, 4×8 elements, 320 to 1000 nm, gain = 50) are employed to detect the imaged light from the optical assembly. The photosensitive area is 1.6×1.6 mm with a minimum pixel pitch of 2.3 mm. The optical assembly enables a greater than 98% of photon reaching to the sensitive area for all APD pixels. In the detector module, a 64-channel pre-amplifier circuit, four quadrant circuit boards, four vacuum interface boards, and 64 fin boards are sealed within a $490 \times 490 \times 200$ mm metal box. The pre-amplifier circuit board is functional for a flexible gain setting, signal filtering and amplification. A picture of the APDs and pre-amplifier circuit is shown in figure 4(a). The four quadrant boards distributes the 64 channels from the pre-amplifier into every 16 channels, whereby each quadrant board is connected via ribbon cables to the individual vacuum interface board for the remote control and data acquisition. The 64 fin boards are mounted beneath quadrant boards to adjust the voltage offset and frequency composition individually. A thermal-electric cooler stabilizes the interior temperature at $-20°C$ aiming to minimize the electronic noise (e-noise) during the operation.

Because the BES optical assembly is under manufacturing, the detector noise measurement is performed by illuminating a green LED ($\lambda \approx 520\ to\ 550$ nm) light through an optical assembly using a band-pass interference filter with 528 to 530 nm of its 90% transmission. Although the wavelength of the light source and optics are not ideal for the BES, the detector module responses similarly due to the broad spectral response of APDs. Therefore, this noise measurement is able to infer a general noise level for the BES detector module. By changing the light intensity, both the dark noise and the photon noise are digitized using a D-Tecq digitizer (ACQ482ELF, 16-bit, 16 channels). Figure 5 shows the noise spectra at different levels of light intensity. The dark noise is measured by operating the APD arrays and pre-amplifier circuit without emitting any light from the optical module. The power spectral density (PSD) varies from $0.6 \times 10^{-7}\ V^2/Hz$ at $f \leq 600$ kHz to around $2 \times 10^{-7}\ \mathrm{V}^2/\mathrm{Hz}$ at 1 MHz. By increasing the light intensity up to 12.2 nW, the photon noise gradually becomes dominant to about $4 \times 10^{-7}\ V^2/Hz$ over the entire frequency range. This noise measurement gives us an impression of the minimum detectable signal by the detector, however, since the noise is naturally uncorrelated between two measurements it can be significantly suppressed by calculating the cross-power of two BES channels for the experimental data.

To demonstrate the capability of the optical detector and electronics amplification system, the first generation of a nearly identical detector module as that planned for the W7-X BES detector has been implemented in the charge exchange imaging (CXI) system on DIII-D for pedestal localized carbon density fluctuation measurements [19]. Figure 6 shows the time-resolved auto-power spectrum for the CXI channel 11 located at the pedestal region in a high-confinement mode (H-mode) discharge. The H-mode starts at about 3.4 s in this plasma, as indicated by a nearly instantaneous drop of the D_α signal. Edge-Localized Modes (ELMs) behave as intermittent spikes in the D_α signal, which induces rapid particle and thermal transport bursts from the H-mode pedestal [20]. During the H-mode, a fluctuation mode in the 30-50 kHz range emerges, coexisting with a low frequency mode below 10 kHz in the spectrum. Although the investigation of fluctuation modes is beyond the scope of this paper, the CXI spectral response in figure 6 demonstrates that the detector module is fully capable of achieving adequate signal-to-noise and sufficient time-resolution for the planned fluctuation measurements of the W7-X BES system. Moreover, the APD quantum efficiency (QE) is about 82% at 529 nm for the CXI measurement, whereas $QE \approx 85\%$ at 656 nm for the W7-X BES system.

2024 JINST 19 P11004

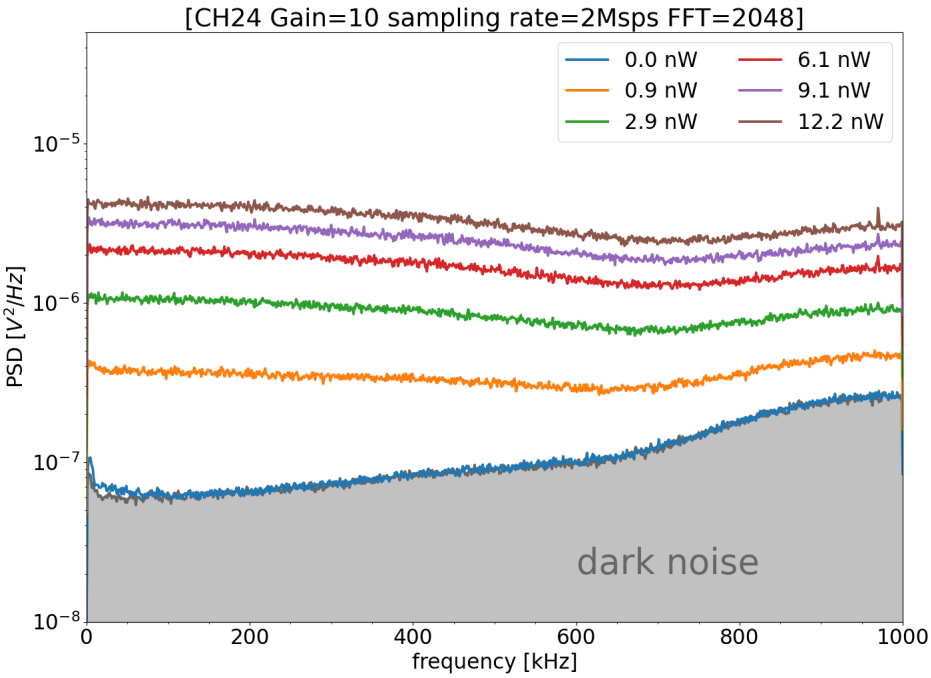

Figure 5. Power spectral density (PSD) of noise measurement using a green LED ($\lambda \approx 550$ nm). The gray area shows the dark noise level when no light is emitted through the APD array. The data are digitized using the D-Tacq digitizer. The gain of the amplifier is 10, sampling rate is 2 Msps, and the points for Fourier transform (fft) is 1024.

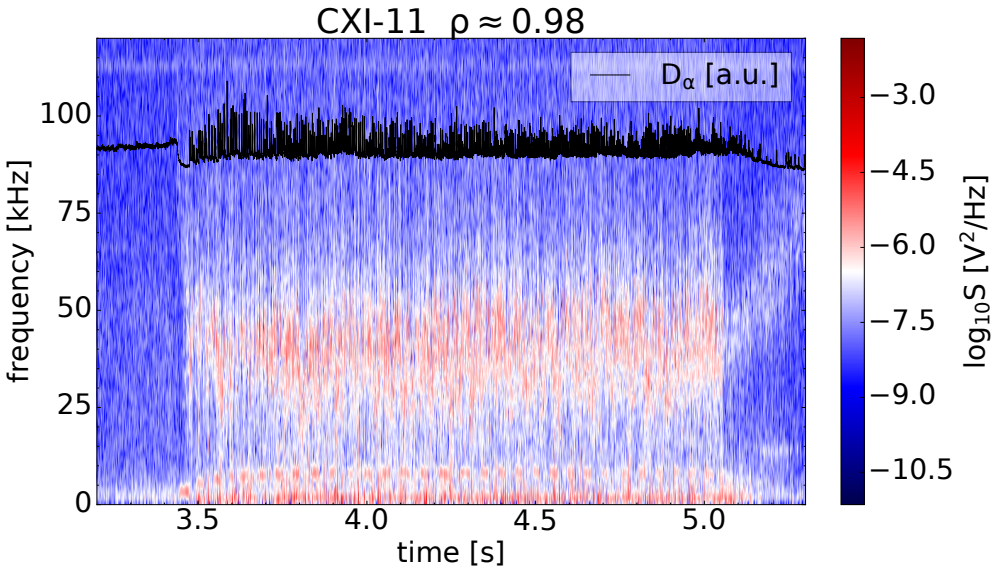

Figure 6. Carbon density fluctuation spectrum that is measured by the charge exchange imaging system (CXI) at the H-mode pedestal region in DIII-D. The time trace of D_α signal is depicted in the black line. The CXI measurement is performed using the first generation of a very similar detector module to the W7-X BES detector.

2024 JINST 19 P11004

4 BES capabilities for 2D turbulence measurement

The spatial resolution of BES system can be assessed via the Point Spread Function (PSF) and Spatial Transfer Function (STF) calculations, which take into account multiple effects including the BES optical viewing geometry, neutral beam density profile, atomic excited state lifetime effect, and the magnetic configuration [21]. A 2D image convolution along a given BES LoS is required for the PSF calculation due to the fact that the fast beam velocity induces a finite lifetime of excited beam atoms, resulting in a downstream decline of emission. The effective lifetime of excited state can be solved by using a multi-state collisional transition model [8], which estimates an exponential decay of the excited state populations along the projection direction of the neutral beam. On W7-X, the lifetime for the excited state of $n = 3$ is about 2.25 ns for a typical plasma density of $6 \times 10^{19} m^{-3}$, which means that with a 60 keV Hydrogen beam, the excited atoms would travel downstream about 0.7 cm. This exponential decay in the cone of emission is convolved with the obtained fiber image on the successive plane, resulting in a radially outward tail and deformed fiber image [22]. The convolved 2D image is then represented by the image on the neutral beam axis via the magnetic field line tracing. This procedure is necessary because the turbulent eddies are assumed to propagate along the toroidal magnetic field line. The magnetic flux curvature could result in a misalignment of the BES LoS, yielding an expansion of the sample volume in both poloidal and toroidal directions.

The rotational transform (ι) profile on W7-X depends on the magnetic field configuration whereas the last-closed flux surface (LCFS) and magnetic island chains are adjusted accordingly [23, 24]. As a consequence, the coverage of the BES LoS changes with respect to the magnetic topology. Figure 7 depicts the PSF calculations for the 8×8 BES LoS grid in standard (EJM+252, edge $\iota = 1$) and high−ι (FTM+252, $\iota > 1$) configurations. In the FTM configuration in figure 7(b), the outermost BES LoS move to the scrape-off-layer, and the fiber images remain similar to the one in the EJM configuration. Note that the LoS grid is rotated by about 22.5° to follow the normal and bi-normal magnetic field directions, aiming to minimize the effect of flux surface misalignment. The ideal BES spots are labeled as black points whereas the PSF spreads out each spot at different extent forming a finite-volume fiber image, where the image smears along radial and poloidal directions. The lower-outer LoS shows a FWHM of about 1.3 cm and 1.1 cm in radial and poloidal extent. The most elongated image appears at the upper-inner LoS, which is mainly due to the magnetic field misalignment that is inferred from figure 2(c). Moreover, the elongated image overlaps with the adjacent LoS in the diagonal, which will reduce the sensitivity of the turbulence measurement. If reducing the overlapped area by increasing the center-to-center spacing of the grid, the upper core channels would move toward the larger magnetic field angle region, resulting in a further elongated image.

The STF describes the intensity distribution of BES measurement in the wavenumber domain, which is the result of 2-dimensional Fourier transform of PSF as a function of the radial (k_r) and poloidal (k_z) wavenumbers. Figure 8 depicts the STF images for the four corner channels of BES LoS grid. It is found that the STF images are elongated and tilted in the poloidal projection corresponding to the PSF images. The e-folding distance in the upper inboard channel is $k_r \approx 1.1\,\mathrm{cm}^{-1}$ and $k_z \approx 2.8\,\mathrm{cm}^{-1}$, whereas the lower outboard channel extends to $k_r \approx 2.5\ cm^{-1}$ radially and the k_z slightly reduces to $2.6\ cm^{-1}$. The measurable k_r and k_z coverage is determined by both the 22.5° rotation of LoS grid and the 1.56 cm spacing of the BES LoS grid. In the W7-X discharge XP:20181016.037, the ion temperature rises up to $1 \sim 1.2$ keV at $\rho = 0.75$, and the maximum $k_\perp \rho_i$ is estimated to be $k_\perp \rho_i \approx 0.4$ for the 1.56 cm spacing of BES grid, here the ion gyroradius is $\rho_i = 2\pi\sqrt{T_i m_i}/eB$. A higher $k_\perp \rho_i$ is accessible with a higher T_i, or smaller grid separation.

2024 JINST 19 P11004

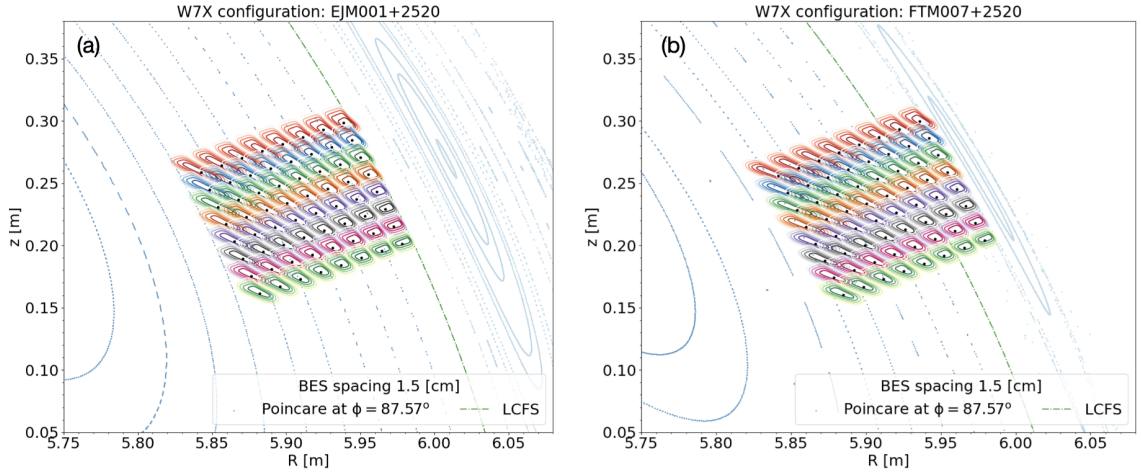

Figure 7. PSF calculations in (a) the standard configuration (XP:20180919.039 at 3.6 s) and (b) high-ι configuration (XP:20180822.013 at 8.6 s) for the 8×8 BES LoS grid at the toroidal angle of 87.57°. The plasma parameters are taken from the NBI discharge on W7-X. The black dots indicate the ideal center of sighlines. The Poincaré figure is shown as light blue dots and the LCFS is indicated by the green dashed line.

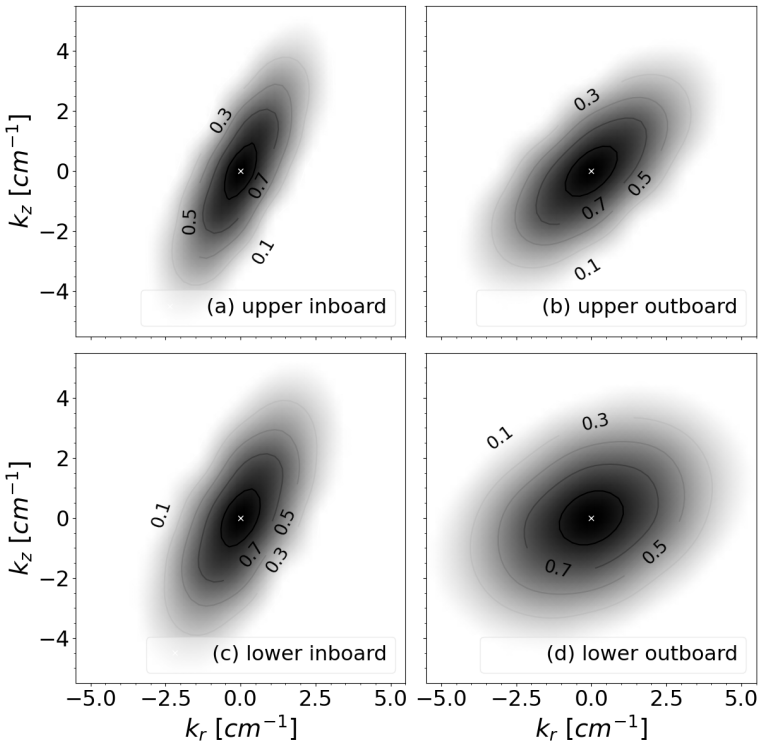

Figure 8. STF calculation of BES LoS at corner pixel. The center of ($k_r = 0$, $k_z = 0$) is labeled as the white cross, and the level of STF amplitude is indicated by the value on the contour.

2024 JINST 19 P11004

5 Spectral isolated beam radiance and detectable fluctuation level estimations

The pyFIDASIM code, which is translated from the FIDASIM [25] using the python interface, is applied to calculate the beam radiance spectrum, and the as-manufactured band-pass interference filter is applied to calculate the beam radiance. The spectral deposition of beam components are simulated by the pyFIDASIM code using the BES LoS geometry and plasma parameters from an NBI discharge on W7-X. This simulation validates the specification of the interference filter in the semi-telecentric optics, which is a compromise aimed at maintaining the majority of beam energy components within the pass-band while blocking the main thermal CX that could contaminate the spectrum due to the small Doppler shifts. The as-manufactured interference filter determines the 10% cutoff at $\lambda_0 \approx 655.7$ nm, and the pass-band is estimated to be shifted in blue by about 0.4 nm at $AOI = 4°$. Results in figure 9 show the beam radiance depositions at off-axis and on-axis pixels for all energy components and the thermal CX ($R = 5.9$ m, $Z = 0.2$ m). The Doppler shifts and the Stark splitting [26] move in blue from the innermost radius to the outermost one. In addition, the thermal CX is broadened towards plasma core, whereas its amplitude decreases by half. It is observed that the AOI leads to a blue-shifted

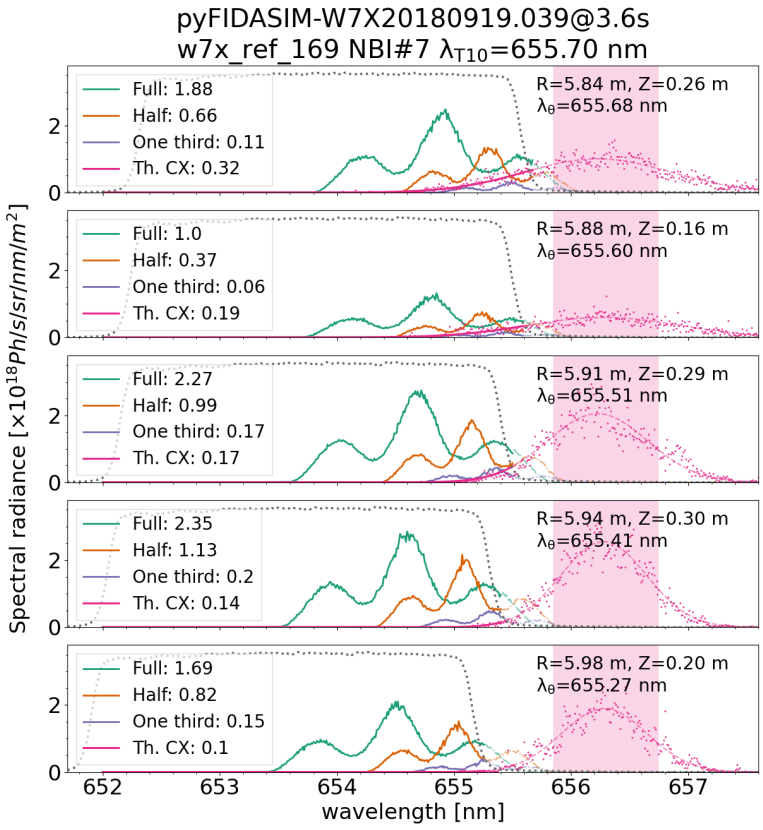

Figure 9. The calculation of the beam radiance depositions at the central and corner BES channels using the pyFIDASIM code. The plasma parameters are taken from the NBI discharge 20180919.039 at 3.6 s in a standard configuration. The as-built interference filter is applied where the 10% transmission of the interference filter is at $\lambda_{\Gamma 10} = 655.7$ nm, and the corresponding cutoff wavelength (λ_θ) due to AOI effect is labeled in each figure. The total radiance in the pass-band of the filter is estimated for the full, half, and one third energy components as shown in the legend with a unit of $\times 10^{18}$ Ph/s/m^2/ster. The magenta area is the estimated bandwidth of thermal CX radiance at $r/a \approx 0.5$ from the charge exchange recombination spectroscopy (CXRS) measurement.

2024 JINST 19 P11004

pass-band of the filter from $\lambda = 655.68$ nm at $AOI = 0.91°$ to $\lambda = 655.27$ nm at $AOI = 3.92°$. Note the thermal CX in pink area is centered at 656.3 ± 0.95 nm which is measured by the charge-exchanged recombination spectroscopy (CXRS) at $r/a \approx 0.54$. It is observed that the bandwidth of thermal CX emission becomes much narrower in the plasma edge region on W7-X, therefore the interference filter is capable to block the thermal CX emission to a negligible level for BES measurements.

In figure 9 the spectral isolated beam radiance is calculated in the range of $1.4 \sim 3.7 \times 10^{18}$ photons/s/m^2/ster whereas the thermal CX in the pass-band is an order lower at about $0.1 \sim 0.32 \times 10^{18}$ photons/s/m^2/ster, that anticipates a net beam intensity of $1.2 \sim 2.7 \times 10^{18}$ photons/s/m^2/ster for the range of beam densities across the BES field of view. The étendue in the detector lens module can be calculated by multiplying the fiber area with its NA value, yielding an étendue of about $0.07\,\text{mm}^2 \cdot \text{ster}$. Assuming a maximum transmission loss of 3 dB in the BES lens assembly, the total emission power delivered to the APD pixel is expected at $7 \sim 9$ nW. For the detector module, the instantaneous signal-to-noise ratio (SNR) is calculated as:

$$\text{SNR} = I_p / N_{\text{rms}} \tag{5.1}$$

where $I_p \approx 1.89 \times P_{\text{inc}} \times G \times \text{QE}$ is the photocurrent on the APD pixel (P_{inc} is the incident power, G is the gain factor of the APD, and QE is quantum efficiency of the APD diode). The N_{rms} is the root-mean-square (RMS) noise of the pre-amplifier circuit and diode, and can be calculated as:

$$N_{\text{rms}} = \sqrt{(N_{\text{diode}} + N_{\text{TIA}})/G^2 \times \text{BW}}, \tag{5.2}$$

where N_{diode} results from the dark current and photocurrent of the APD diode, and N_{TIA} is the trans-impedance amplifier (TIA) noise which is dominated by the thermal noise of the pre-amplifier circuit and is a function of frequency and temperature [27]. Figure 10(a) calculates the instantaneous SNR at −20°C with a bandwidth (BW) of 1 MHz. It is seen that the SNR is in a range of 60 to 90 at $P_{\text{inc}} = 10$ nW when Gain ≥ 5. Assuming a density fluctuation level of $\tilde{n}_e/n_e = 0.5\%$ at 150 kHz

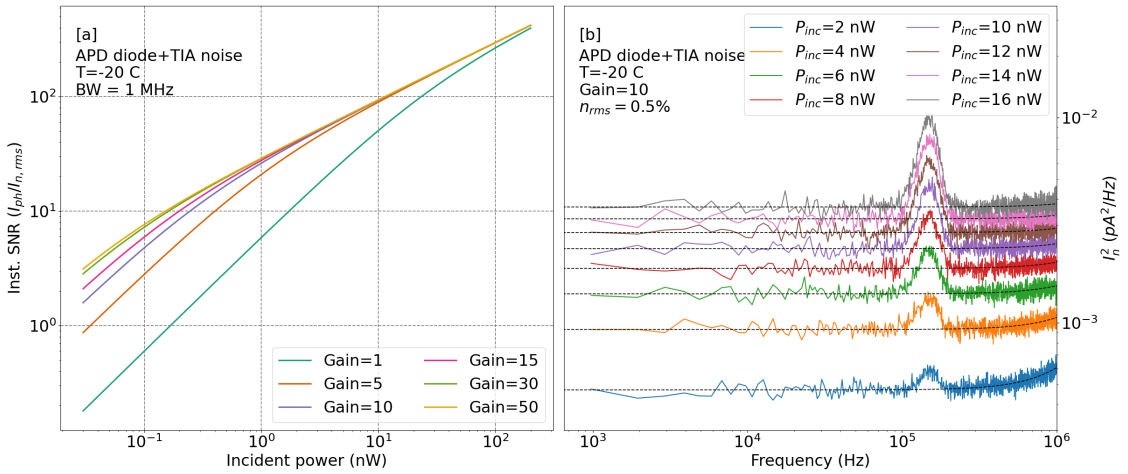

Figure 10. (a) Instantaneous signal-to-noise ratio (SNR) for APD and trans-impedance amplifier (TIA) in the detector module with a bandwidth of 1 MHz at −20°C. The APD gain tunes form 1 up to 50. (b) Frequency-resolved spectrum with the gain at 10 and temperature at −20°C, assuming a rms density fluctuation level of $n_{\text{rms}} = 0.5\%$ at 150 kHz (50 kHz full-width at half-maximum. The incident power scans from 2 nW to 16 nW as indicated by the color, and the black dashed line depicts the noise level in each power step.

2024 JINST 19 P11004

with a full-width at half-maximum (FWHM) bandwidth of 50 kHz is superposed on the detector noise source, a simulated frequency spectrum in figure 10(b) indicates that as the $p_{\mathrm{inc}} \geq 4$ nW, the 150 kHz fluctuation can be identified from the noise level, although with increasing the incident power the noise level increases over the entire frequency range. When P_{inc} is low the noise increases significantly at $f \geq 400$ kHz, which would make the fluctuations difficult to discern on the frequency spectrum. Therefore, the density fluctuation in the ITG/TEM range is measurable by the BES diagnostic for $\tilde{n}_e/n_e \geq 0.5\%$ at $f \leq 400$ kHz.

6 Summary

We describe the detailed structure of the BES diagnostic, including the in-vessel geometry of the field of view, optical lens assembly, and the detector module. The capabilities of BES diagnostic for 2D density fluctuation measurements are evaluated based on the optical throughput and the performance of the detector. It is shown that using the 8×8 LoS grid, BES is sensitive to ITG / TEM turbulence up to $k_\perp \rho_i \approx 0.4$ at $r/a = 0.75$. The PSF and STF calculations show a reasonable spatial resolution in the (R, Z) and $(k_r,\ k_\theta)$ domains. However, an extremely elongated spot image appears on the upper core LoS overlapping with adjacent LoS due to the misalignment of its LoS with the magnetic field. The optical throughput estimation is performed via the pyFIDASIM simulation using the beam viewing geometry and plasma parameters of the NBI discharge. It indicates that the beam radiance in the pass-band is sufficient to be resolved from the BES measurement, although the AOI effect alters the pass-band of the optical filter for the beam radiance of BES. Nevertheless, BES is able to measure a fluctuation level as low as $(\tilde{n}_e/n_e)_{\mathrm{min}} \approx 0.5\%$ in a frequency range of $f \leq 400$ kHz, which would provide novel insight for the investigation of ITG turbulence on W7-X. The front-end optical assembly is foreseen to be installed during the W7-X maintenance phase (MP2.2) in 2024–2025, and the experimental measurement of BES is targeted in the later campaign.

Acknowledgments

This work is Supported by U.S. Department of Energy, Office of Science, Office of Fusion Energy Sciences Award Np. DE-SC0019009, DE-FG02-08ER54999 and DE-FC02-04ER54698. This work has been carried out within the framework of the EUROfusion Consortium, funded by the European Union via the Euratom Research and Training Programme (Grant Agreement No. 101052200 — EUROfusion). Views and opinions expressed are however those of the author(s) only and do not necessarily reflect those of the European Union or the European Commission. Neither the European Union nor the European Commission can be held responsible for them.

This report was prepared as an account of work sponsored by an agency of the United States Government. Neither the United States Government nor any agency thereof, nor any of their employees, makes any warranty, express or implied, or assumes any legal liability or responsibility for the accuracy, completeness, or usefulness of any information, apparatus, product, or process disclosed, or represents that its use would not infringe privately owned rights. Reference herein to any specific commercial product, process, or service by trade name, trademark, manufacturer, or otherwise does not necessarily constitute or imply its endorsement, recommendation, or favoring by the United States Government or any agency thereof. The views and opinions of authors expressed herein do not necessarily state or reflect those of the United States Government or any agency thereof.

2024 JINST 19 P11004

References

[1] M.N.A. Beurskens et al., *Ion temperature clamping in Wendelstein 7-X electron cyclotron heated plasmas*, *Nucl. Fusion* **61** (2021) 116072.

[2] G.M. Weir et al., *Heat pulse propagation and anomalous electron heat transport measurements on the optimized stellarator W7-X*, *Nucl. Fusion* **61** (2021) 056001.

[3] B. Geiger et al., *Observation of anomalous impurity transport during low-density experiments in W7-X with laser blow-off injections of iron*, *Nucl. Fusion* **59** (2019) 046009.

[4] C.D. Beidler et al., *Demonstration of reduced neoclassical energy transport in Wendelstein 7-X*, *Nature* **596** (2021) 221.

[5] P. Xanthopoulos et al., *Turbulence Mechanisms of Enhanced Performance Stellarator Plasmas*, *Phys. Rev. Lett.* **125** (2020) 075001.

[6] R.J. Fonck, P.A. Duperrex and S.F. Paul, *Plasma fluctuation measurements in tokamaks using beam-plasma interactions*, *Rev. Sci. Instrum.* **61** (1990) 3487.

[7] G.R. McKee, C. Fenzi, R.J. Fonck and M. Jakubowski, *Turbulence imaging and applications using beam emission spectroscopy on DIII-D (invited)*, *Rev. Sci. Instrum.* **74** (2003) 2014.

[8] I.H. Hutchinson, *Excited-state populations in neutral beam emission*, *Plasma Phys. Control. Fusion* **44** (2001) 71.

[9] S. Bose et al., *Two-dimensional plasma density evolution local to the inversion layer during sawtooth crash events using beam emission spectroscopy*, *Rev. Sci. Instrum.* **93** (2022) 093521.

[10] G.R. McKee et al., *High sensitivity beam emission spectroscopy for core plasma turbulence imaging (invited)*, *Rev. Sci. Instrum.* **77** (2006) 10F104.

[11] G.R. McKee et al., *Turbulence velocimetry of density fluctuation imaging data*, *Rev. Sci. Instrum.* **75** (2004) 3490.

[12] D.R. Smith et al., *Overview of the beam emission spectroscopy diagnostic system on the National Spherical Torus Experiment*, *Rev. Sci. Instrum.* **81** (2010) 10D717.

[13] Y.F. Wu et al., *Development of a 32-channel Beam Emission Spectroscopy diagnostic based on Neutral Beam Injection on HL-2A tokamak*, *Fusion Eng. Des.* **156** (2020) 111734.

[14] Y.F. Wu et al., *Simulation of neutral beam attenuation and its influence to beam emission spectroscopy diagnostic on HL-2A tokamak*, 2018 *JINST* **13** P10026.

[15] X. Qin et al., *Integrated 2D beam emission spectroscopy diagnostic at the Huan-Liuqi-2A (HL-2A) tokamak*, *Rev. Sci. Instrum.* **93** (2022) 103535.

[16] A.R. Field et al., *Beam emission spectroscopy turbulence imaging system for the MAST spherical tokamak*, *Rev. Sci. Instrum.* **83** (2012) 013508.

[17] T. Kobayashi, M. Yoshinuma and K. Ida, *Two-dimensional beam emission spectroscopy for hydrogen isotope negative neutral beam in Large Helical Device*, *Plasma Phys. Control. Fusion* **62** (2020) 125011.

[18] D.R. Smith et al., *Conceptual design and performance predictions for 2D beam emission spectroscopy turbulence measurements at Wendelstein 7-X*, *Rev. Sci. Instrum.* **93** (2022) 073506.

[19] M.R. Major et al., *Pedestal fluctuation measurements with charge exchange imaging at the DIII-D tokamak*, *Rev. Sci. Instrum.* **93** (2022) 113503.

[20] S. Banerjee et al., *Evolution of ELMs, pedestal profiles and fluctuations in the inter-ELM period in NBI- and ECH-dominated discharges in DIII-D*, *Nucl. Fusion* **61** (2021) 056008.

2024 JINST 19 P11004

[21] M.W. Shafer, R.J. Fonck, G.R. McKee and D.J. Schlossberg, *Spatial transfer function for the beam emission spectroscopy diagnostic on DIII-D*, *Rev. Sci. Instrum.* **77** (2006) 10F110.

[22] Y.-C. Ghimand (Kim), A.R. Field, S. Zoletnik and D. Dunai, *Calculation of spatial response of 2D beam emission spectroscopy diagnostic on MAST*, *Rev. Sci. Instrum.* **81** (2010) 10D713.

[23] T. Andreeva et al., *Magnetic configuration scans during divertor operation of Wendelstein 7-X*, *Nucl. Fusion* **62** (2022) 026032.

[24] A. Dinklage et al., *Magnetic configuration effects on the Wendelstein 7-X stellarator*, *Nature Phys.* **14** (2018) 855.

[25] B. Geiger et al., *Progress in modelling fast-ion D-alpha spectra and neutral particle analyzer fluxes using FIDASIM*, *Plasma Phys. Control. Fusion* **62** (2020) 105008.

[26] W. Mandl, R.C. Wolf, M.G. Hellermann and H.P. Summers, *Beam emission spectroscopy as a comprehensive plasma diagnostic tool*, *Plasma Phys. Control. Fusion* **35** (1993) 1373.

[27] G.C. Cosby, *Beam Emission Spectroscopy Analysis*, M.Sc. thesis, University of Wisconsin-Madison, Madison, WI (1992).

2024 JINST 19 P11004